Chemical Engineering Journal 488 (2024) 150951

Contents lists available at ScienceDirect

Chemical Engineering Journal

journal homepage: www.elsevier.com/locate/cej

Assembling bifunctional ceria-zirconia electrocatalyst for efficient electrochemical conversion of methane at room temperature

Nicole Boghosian Patricio [a], Juliano Carvalho Cardoso [a,b], Márcia Tsuyama Escote [c], Alexandre José de Castro Lanfredi [c], Abhaya Datye [d], Hien Pham [d], Caue Ribeiro [e], Fabio Coral Fonseca [a,*], Elisabete Inacio Santiago [a,*]

[a] Nuclear and Energy Research Institute, IPEN-CNEN, São Paulo, Brazil
[b] UFMS, Federal University of Mato Grosso do Sul, Campo Grande, Brazil
[c] CECS, Federal University of ABC, Santo André, Brazil
[d] University of New Mexico, Albuquerque, US
[e] Nanotechnology National Laboratory for Agriculture (LNNA), Embrapa Instrumentation, São Carlos, Brazil

ARTICLE INFO

Keywords:
Methane conversion
Electrocatalysts
Ceria-zirconia
Bifunctional catalyst
Methanol

ABSTRACT

The electrochemical conversion of methane to C2 compounds at room temperature is reported using CeO_2-ZrO_2 electrocatalysts. The mixed oxide electrocatalysts produced methanol, ethanol, and acetone, along with traces of acetaldehyde and isopropanol, under a polarization of 1.2 V with ~ 50 % Faradaic efficiency. Detailed characterization of the CeO_2-ZrO_2 revealed the formation of nanoparticles (7–9 nm mean size) composed of ceria-zirconia solid solution or a mixture of ceria with both tetragonal and monoclinic zirconia polymorphs depending on the assembling configuration of the electrocatalyst. Samples with separated phases and limited solid solution formation showed the highest electrochemical activity, indicating that an optimal assembly of ceria and zirconia was crucial to achieving efficient conversion with high Faradaic efficiency and selectivity. Such high electrochemical activity observed for the phase separated CeO_2-ZrO_2 electrocatalyst suggests that a synergic effect between ceria and zirconia is required for the critical reaction steps, such as the activation and partial oxidation of methane. The experimental results point to credible routes to efficiently convert methane into valuable chemicals in mild conditions.

1. Introduction

Methane (CH_4) is the simplest alkane and serves as the fundamental building block for most bulk organic compounds on Earth. It constitutes the primary component of natural gas, accounting for 70 to 90 % of its composition, making it the fastest-growing fossil fuel globally [1,2]. According to the International Energy Outlook 2019 (IEO2019), global natural gas consumption is projected to rise by 40 % from 2018 to 2050, reaching 200 quadrillion Btu [3,4]. However, methane is a potent greenhouse gas (GHG) with a significantly higher impact on the absorption and emission of infrared radiation (IR) compared to CO_2, exhibiting 25 times greater global warming potential on an equimolar basis [1–3]. Typically, methane is flared, converting it into carbon dioxide, which results in the transformation of a potential feedstock into polluting waste. Given the increasing number of natural gas reserves, the development of efficient methane conversion processes has become crucial in recent years. The deployment of technology capable of converting methane into easily storable liquid fuels, such as methanol, while simultaneously reducing greenhouse gas emissions is highly desirable [1,5–7].

Despite the thermodynamics and kinetics of the oxidative C – H bond activation in CH_4 allowing its low-temperature conversion, its high bond dissociation energy (435 $kJ{\cdot}mol^{-1}$) poses a challenge for C – H cleavage reactions via homolytic or heterolytic pathways. These processes suffer from limited selectivity for the desired products, and only a few catalysts can prevent excessive oxidation, leading to the formation of carbon dioxide (CO_2) [8–12]. The main strategies employed to promote methane conversion to other products include biocatalysis, homogeneous catalysis, heterogeneous thermal catalysis, photocatalysis, and electrocatalysis [13]. Electrochemical processes are particularly appealing for low-temperature activation and offer several advantages over purely chemical processes, such as the production of pure

* Corresponding authors.
E-mail addresses: fabiocf@usp.br (F. Coral Fonseca), elisabete.santiago@usp.br (E. Inacio Santiago).

https://doi.org/10.1016/j.cej.2024.150951
Received 19 December 2023; Received in revised form 15 March 2024; Accepted 1 April 2024
Available online 6 April 2024

chemicals, reduction of activation energy, and precise control over product formation through the manipulation of surface free energy and electrode potential [12]. Although methane can be electrochemically converted to methanol with high selectivity, the overall efficiency of the process is often low, demanding new catalysts [14]. For instance, highly reactive metals like platinum (Pt) tend to promote complete oxidation [15,16].

Metal oxides, with their versatile acid-base and redox properties, along with high chemical, thermal, and mechanical stability, hold promise for partial oxidation reactions. Mixed oxides based on zirconia (ZrO_2) in combination with other oxides have been used for direct methane activation [14,17–19]. For example, a bifunctional NiO-ZrO_2 electrocatalyst employed carbonate ions (CO_3^{2-}) to activate methane via oxygen insertion (O^{2-}). ZrO_2 functions as a surface Lewis acid site, capable of accepting electrons and facilitating CO_3^{2-} adsorption, while NiO activates methane at room temperature [14]. Similar behavior has been observed for Co_3O_4/ZrO_2, further confirming the role of ZrO_2 [20].

By considering that ceria (CeO_2) has been validated as an excellent catalyst for CH_4 oxidation [14,21–24], because of its capacity to promote oxygen diffusion through oxygen vacancies, it can be tuned to an adequate electrocatalyst to regulate the methane conversion reaction. As the selectivity of the products depends on the electrocatalyst's efficiency in controlling the reaction with CO_3^{2-} and ZrO_2 was shown to play a role in the CH_4 activation, we can use zirconia as a modifier for the active ceria. Therefore, the present study explores mixed CeO_2/ZrO_2 electrocatalysts with distinct microstructural configurations, such as solid solutions and mixed oxides, which can efficiently react with methane to form value-added compounds under mild conditions. Experimental results indicate that ceria-zirconia effectively activates CH_4, leading to sustainable and controlled methane conversion, with a preference for methanol, achieved through a controlled microstructure that maintains a subtle separation between the Lewis acid sites of zirconia and the active oxygen species of ceria.

2. Materials and methods

2.1. Synthesis of CeO_2-ZrO_2 bifunctional electrocatalysts

A microwave-assisted hydrothermal (MH) method was used to synthesize the electrocatalysts. Zirconyl nitrate hydrate ($N_2O_7Zr{\cdot}xH_2O$, Sigma-Aldrich) and cerium nitrate hexahydrate ($CeN_3O_9{\cdot}6H_2O$, Sigma-Aldrich) were used as precursor salts and potassium hydroxide (KOH, Synth) as a precipitating agent. All reactants were used as received from freshly opened recipients. The electrocatalysts were synthesized with a nominal Ce:Zr molar ratio of 1:2, 1:1, and 2:1. All reactants were dissolved in ultrapure water (UPW, Milli-Q) under constant stirring at room temperature for 30 min. Subsequently, the precursor solution was taken to the MH (Milestone SynthWave) reactor, set at 200 °C for 30 min and 1500 W of power under an initial pressure of 45 bar for all runs. Three different microstructural configurations were studied, as shown in the schematics of Fig. 1. The $Ce_xZr_yO_z$ (CZ) sample results from the simultaneous synthesis of ceria and zirconia by mixing both precursors in the same MH reaction medium, forming a solid solution. Two additional samples were prepared: ZrO_2 particles (preformed) with CeO_2 addition (pZC) and ceria particles (preformed) with zirconia (pCZ). These electrocatalyst samples were synthesized by separating the oxide precursors in a two-step MH synthesis. Firstly, the nanoparticles of one oxide (ceria or zirconia) were synthesized following the same procedure described for the CZ sample. In the second step, the previously prepared oxide nanoparticles (e.g., ceria) were mixed with the precursor solution of the second oxide (e.g., zirconia) to form the phase-separated electrocatalyst (e.g., pCZ). The two MH synthesis steps were run with the same parameters to produce the electrocatalyst.

After each MH reaction, including ceria and zirconia nanoparticles, the precipitates were centrifuged and thoroughly washed out using Milli-Q standard water until reaching pH = 7 to remove all chemical residues. Finally, the materials were dried in an oven at 80 °C for 24 h.

2.2. Characterization of electrocatalysts

The phase analysis of the prepared powders was performed in an X-ray diffractometer (XRD) D8 Focus Bruker AXS with Cu K-alpha radiation (λ = 15.4056 nm), over an angular range varying from 10° to 110°, at 0.002°angular step and 3 s/step counting rate.

Rietveld analyses were performed in X-ray diffraction data. The FULLPROF software (2021) was used to perform the refinements, using Thompson-Cox-Hastings pseudo-Voigt and Chebyshev polynomial functions to fit the shape and background of these data, respectively. From preliminary analysis, the X-ray patterns were indexed with three crystallographic phases: cubic CeO_2 (ICSD 24887), tetragonal ZrO_2 (ICSD 66785), and monoclinic (ICSD 417639), then the initial structural model used the parameters described in the ICSD 24887, ICSD 66785, and ICSD 417639 files. The refinements evaluated the cell parameters and the amount of each phase.

Wavelength Dispersive X-ray (WDX) analysis of the samples was performed on a Rigaku Supermini 200 X-ray fluorescence spectrometer with a Pd tube (50 kV, 4 mA). Specific surface areas were determined by N_2 physisorption method at 77 K (Micromeritics ASAP-2020 Surface Area Analyzer) according to the Brunauer-Emmett-Teller (BET) method. Before the experiment, the samples were subjected to thermal pretreatment at 300 °C for ~16 h (100 mmHg—Micromeritics VacPrep 061) for surface degassing and stored in a vacuum chamber.

High-resolution transmission electron microscopy (HR-TEM) was carried out using a FEI TECNAI G2 F20 HR-TEM microscope at 200 kV. The samples were prepared by using isopropanol dispersion of the electrocatalyst powders. Subsequently, 3 μL of the dispersion was dripped onto a lacey carbon film (300-mesh) on a Cu TEM grid. To obtain atomic-scale images and EDS mapping, we used an aberration-corrected

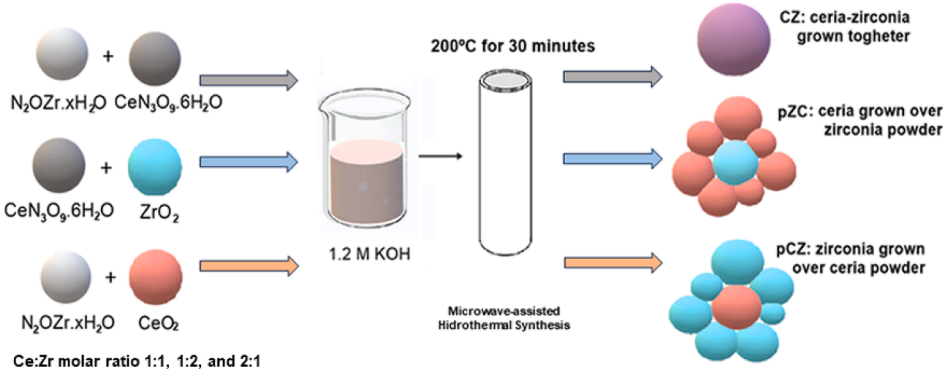

Fig. 1. Schematics of the synthesis of ceria-zirconia: representation of CZ, and the second step of the synthesis for the phase-separated samples pCZ and pZC.

scanning-TEM (STEM) JEOL 200 CF NeoArm equipped with dual EDS detectors. Both bright field and annular dark field images were recorded.

X-ray photoelectron spectroscopy (XPS) determined the catalyst surface chemistry using an Omicron surface analysis station coupled to a SPHERA hemispherical analyzer and a DAR 400 Al Kα x-ray source (hν = 1486.7 eV). The binding energy scales were calibrated based on the C-C contribution of carbon 1 s peak at 284.8 eV.

2.3. Preparation of gas diffusion electrodes (GDE)

The synthesized materials were deposited on carbon paper (Toray, TGP-H-60) (2.0 x 2.0 cm) using a spray gun. A precursor ink with catalyst loading of 1.0 mg cm^{-2} using a weight proportion of 70 % for electrocatalyst and 30 % for Nafion® D-520, used as the binder, was employed for the catalyst layer deposition. To facilitate the deposition, 1 mL of Milli-Q standard water and 9 ml of isopropanol were added to the solution. The loading control was performed by gravimetry, weighting before and after the electrocatalyst ink deposition, and drying.

2.4. Methane electrochemical conversion

Electrooxidation runs were carried out using a single-compartment stainless steel reactor (external dimensions of 9x9x7 cm^3 and wall thickness of 1 cm) with 100 mL solution capacity. In the reaction chamber, a circular cavity at the bottom facilitates mechanical agitation during electrochemical reaction. The spacing between electrodes in the reactor was 1 cm. Initially, nitrogen was bubbled in 0.1 mol/L Na_2CO_3 solution, pH = 12, for 30 min, followed by methane flow at 200 mL/min flow rate for 60 min before cyclic voltammetry tests, then kept constant during chronoamperometry measurements to ensure saturation.

The gas diffusion electrodes were connected as the working electrode, while a platinum wire was used as a counter electrode and Ag/AgCl in KCl 3.0 mol/L as the reference electrode. Cyclic voltammograms and chronoamperometry measurements were performed in a potentiostat/galvanostat Autolab model 102 N. Cyclic voltammograms were collected before each chronoamperometry measurement to define oxidation peaks and their respective potentials. For this purpose, a 20 mV/s scan rate was used in a range of 0.1 to 2.0 V before and after CH_4 bubbling. The defined peak potentials were then applied in chronoamperometry experiments. At each fixed potential, the electrical current was monitored for a time interval of up to 2 h, totalizing 4 h of chronoamperometric runs. After a one-hour time interval at each fixed potential, 3 mL electrolyte aliquots were collected to identify and quantify the products generated by methane oxidation.

The identification and quantification of the products obtained after the electrochemical experiments were performed through gas chromatography in an Agilent model 7890B GC coupled to a mass detector (MS) and flame ionizer detector (FID), with a HP-PLOT/U column (30 m x 0.535 mm x 20 μm). The headspace method was used. For that, 3 mL aliquots were collected and transferred to 20 mL glass vials sealed with rubber septa. Such containers were left in a water bath system for 5 min at 80° C. Finally, a volume of 1 mL was injected into the chromatograph to fill the injection loop. The chromatographic conditions were defined as a temperature gradient of 35° for 4 min, followed by a heating ramp of 30 °C/min to 130 °C, maintained for 10 min.

The faradaic efficiencies (FEs) were calculated according to Equation (1),

$$\eta = \frac{nFN}{Q} \quad (1)$$

where n is the number of electrons involved in the reaction for each product, F is Faraday's constant, N is the number of mols from the process obtained from GC analysis, and Q is the charge after 1 h of electrochemical experiment.

3. Results and discussion

3.1. Characterization of electrocatalysts

Fig. 2 shows the X-ray diffractograms for the ceria-zirconia samples. Ceria is crystallized in the cubic phase (PDF34-394), while zirconia peaks were indexed to monoclinic (PDF 37–1484) and tetragonal (PDF 50–1089) polymorphs. Both the pZC and pCZ samples exhibit a mixture of ceria and zirconia crystalline phases. The indexed peaks of both ceria and zirconia polymorphs confirmed the coexistence of the two oxides. Differently, the XRD patterns of the CZ samples show peaks indexed to the cubic $Ce_{0.6}Zr_{0.4}O_2$ phase (PDF 38–1439). The XRD patterns of the CZ series exhibit broad peaks with 2θ positions shifting depending on the relative composition of the oxides. This result indicates the formation of ceria-zirconia solid solutions for the CZ samples, consistently with the mixing of both ceria and zirconia precursors during the synthesis. The analysis of the XRD patterns is complex in this Ce:Zr system because it is a multiphase system with a relatively small size of the particles and possible formation of solid solutions in a broad range of compositions. Thus, selected samples were further analyzed using Rietveld refinement.

Rietveld refinement was used to quantify crystalline phases and solid solution formation in the ceria-zirconia samples. The refinements for the Ce:Zr 2:1 pZC, pCZ, and CZ samples evidenced ceria and zirconia (both tetragonal and monoclinic) oxides with fitted crystallographic parameters listed in Tables S1, S2, and S3, respectively. The refinement of the pCZ sample required a tiny mass fraction (0.4 %) of CeO_2:ZrO_2 solid solution along with ceria and the zirconia polymorphs. Rietveld refinements for the CZ samples evidenced ceria-zirconia solid solution as the major phase. Interestingly, the ceria lattice parameters of both pCZ and pZC were close to the nominal value reported for the CeO_2 and indicated that no solid solution was formed, irrespective of the relative concentration of the oxides. The CZ lattice parameters shown in Table S3 are consistent with the $Ce_{0.6}Zr_{0.4}O_2$ solid solution composition.

Therefore, XRD data reveals a strong dependence of the phase distribution on the synthesis of the samples. Mixing ceria and zirconia precursors in CZ samples results in an extensive solid solution formation, prevailing the cubic symmetry of the ceria. On the other hand, when first nucleating nanoparticles of one oxide, either zirconia or ceria, followed by the assembling of the second one, as in the pCZ and pZC series, the separation of the ceria and zirconia polymorphs is promoted.

Detailed electron microscopy analyses were carried out to unveil the phase assembling of the studied electrocatalysts. Fig. 3 shows the high-resolution transmission electron microscopies (HR-TEM) for pZC, pCZ, and CZ electrocatalysts with Ce:Zr ratio 2:1. The pZC and pCZ samples show agglomerated particles with similar shapes, both cubic and spherical particles, with calculated average particle size 7.6 and 8.9 nm, respectively. The CZ sample has finer particles and a more agglomerated morphology with a calculated average particle size 5.4 nm. The BET surface area values for the CZ, pCZ, and pZC samples are comparable, with the CZ sample exhibiting a slightly higher specific surface area (153 m^2/g) due to its smaller particle size. In contrast, the phase-separated samples pCZ and pZC have similar surface area values: 131 m^2/g and 126 m^2/g, respectively.

The Fast Fourier Transform (FFT) analysis from pZC, pCZ, and CZ STEM images (Fig. S1) provided valuable information about the d-spacing values of crystalline planes of the synthesized oxides. For the pZC sample the FFT analysis revealed d-spacing values of 0.313 nm, 0.277 nm, and 0.196 nm, corresponding to the (1 1 1), (2 0 0), and (2 2 0) planes of cubic ceria, respectively. The d-spacing values of 0.299 nm and 0.182 nm, representing the (0 1 1) and (1 1 2) planes for tetragonal zirconia, respectively (Table S4). Additionally, a few spots at 0.270 nm were attributed to (−1 1 1) planes of monoclinic zirconia. The FFT analysis of pCZ revealed d-spacing values that were associated with ceria and tetragonal zirconia. On the other hand, the CZ sample exhibited the planes of cubic ceria reflecting the formation of the $Ce_{1-x}Zr_xO_2$ solid solution. Such findings further confirm the observed phase

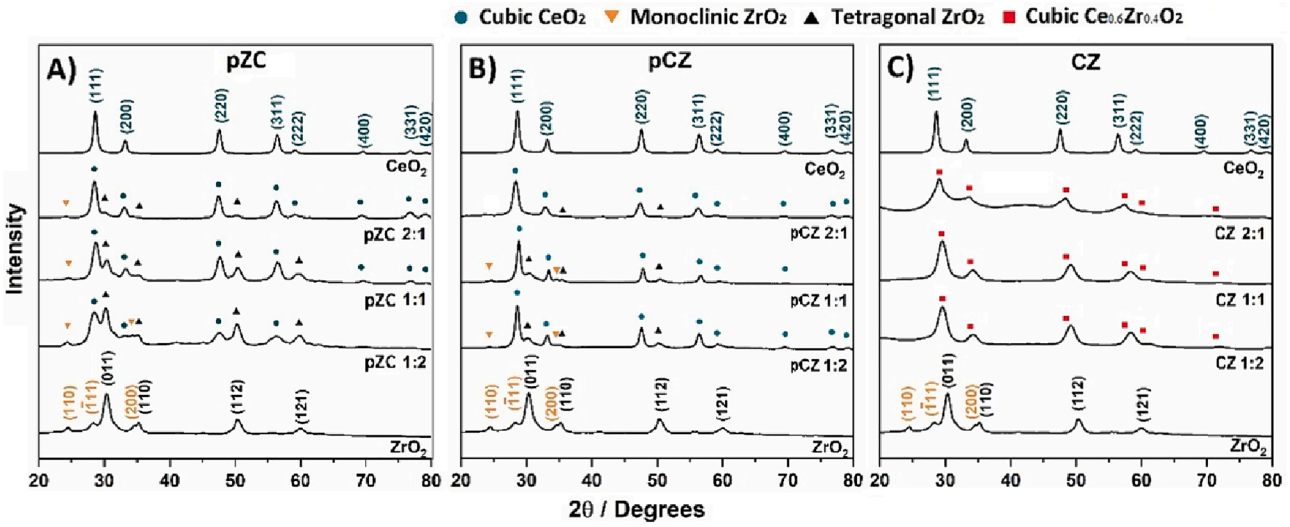

Fig. 2. X-ray diffractograms for (a) pZC, (b) pCZ, and (c) CZ. The XRD of the synthesized CeO2 and ZrO2 are shown as references.

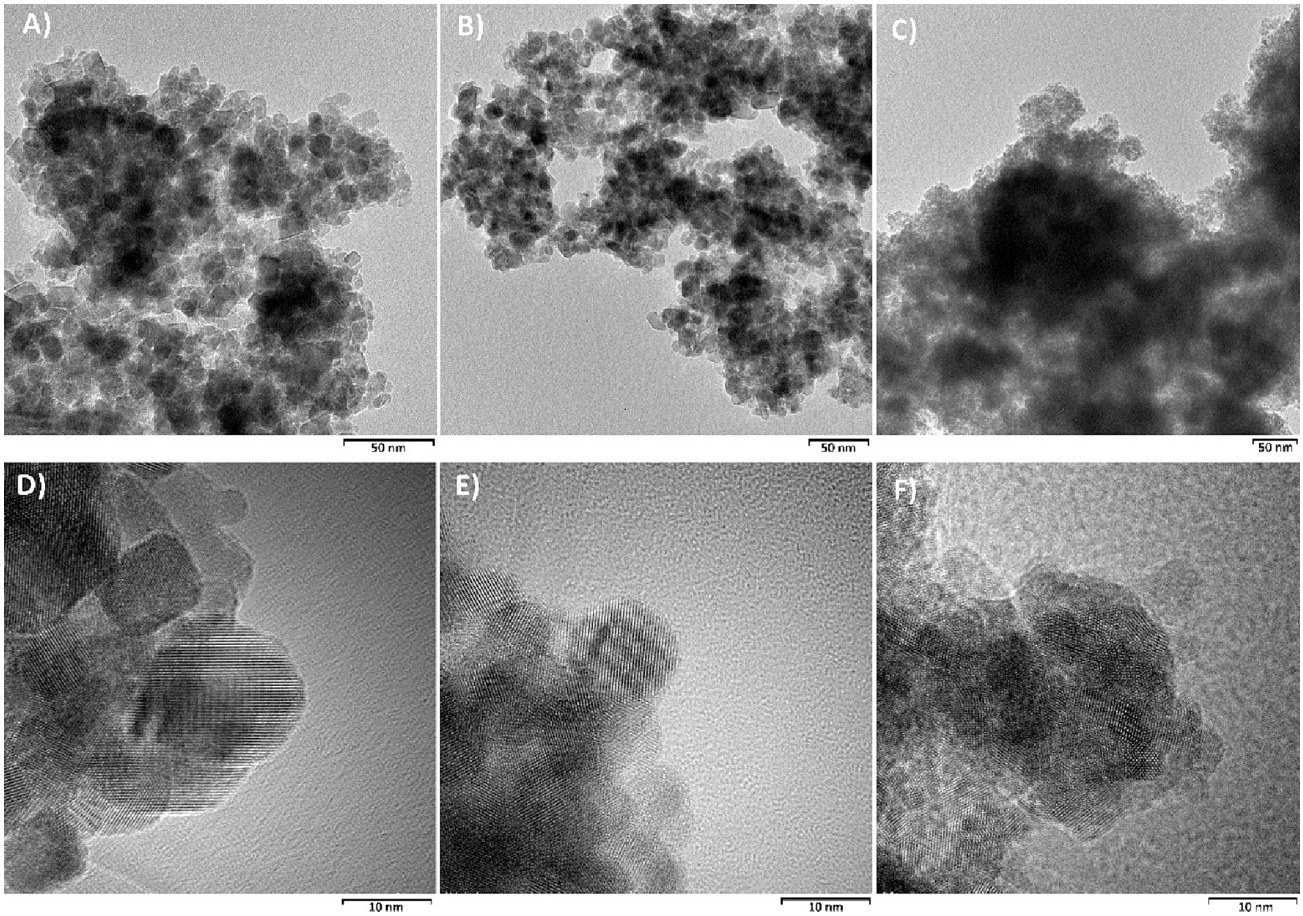

Fig. 3. HR-TEM images for the pZC (A, D), pCZ (B, E), and CZ (C, F) samples with the Ce:Zr ratio 2:1.

distribution dependence on the electrocatalyst synthesis detected by the XRD analysis.

To better distinguish the chemical composition of the nanoparticles, the ceria-zirconia electrocatalysts were further investigated by the high-resolution STEM-EDS mapping analyses depicted in Fig. 4. The EDS analyses were performed in four randomly chosen regions of each sample, and the results in Fig. 4 show representative regions of each sample. The EDS maps revealed significant differences between the samples. Both pCZ and pZC exhibited a heterogeneous distribution of ceria and zirconia, with some composition deviations depending on the region analyzed. Some nanometric particle agglomerates displayed higher concentrations of one oxide, while other regions of the same sample had composition that closely matched the nominal ratio. The phase separation is clearly observed for the samples pZC and pCZ, in which nanometric regions rich in Zr and Ce are evident and in perfect agreement with the XRD data. Such microstructures are consistent with

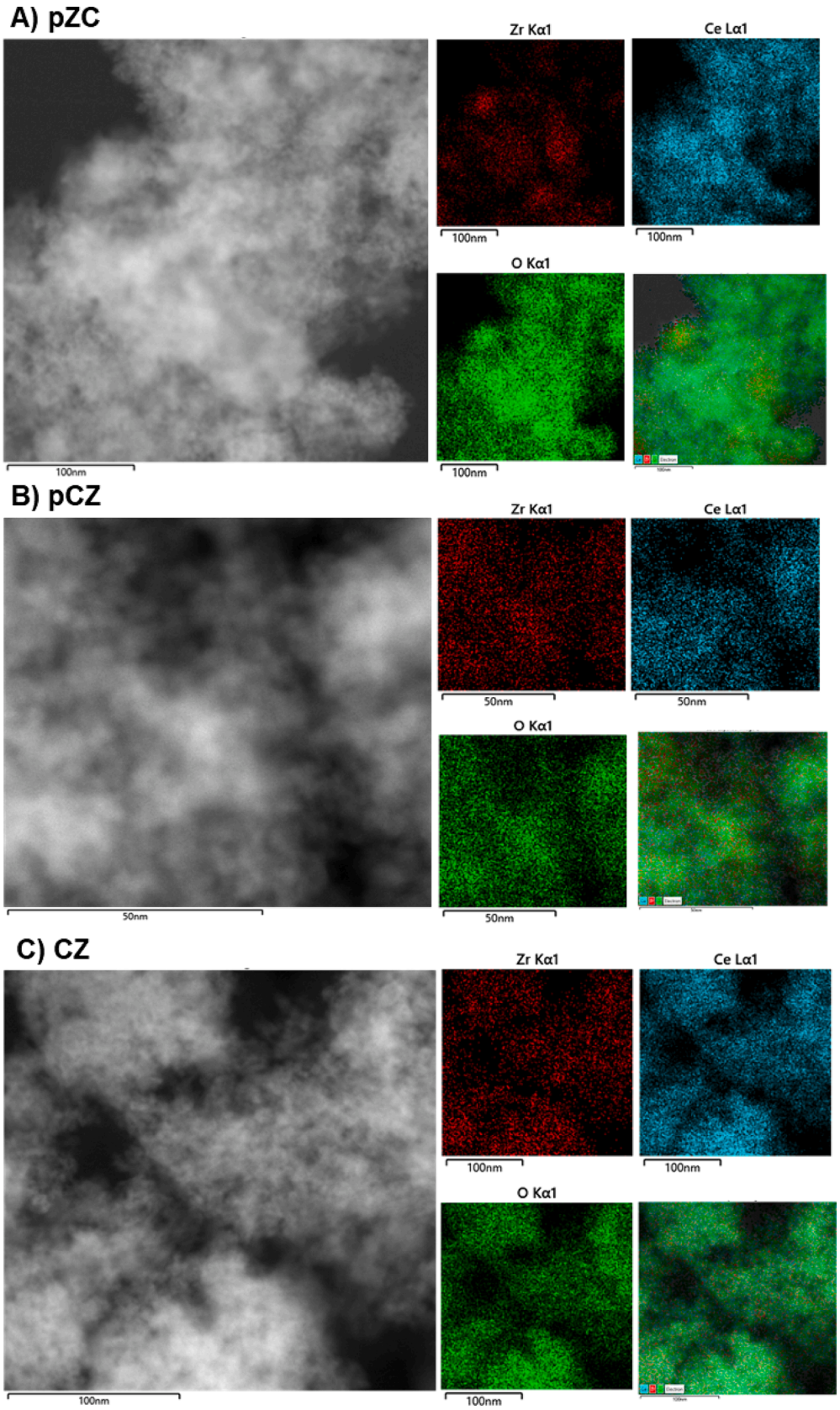

Fig. 4. STEM images with EDS analysis for (A) pZC, (B) pCZ, and (C) CZ samples with Ce:Zr ratio 2:1. Left panel shows the electron image in Annular Dark Field mode, and at right panel the corresponding EDS mapping for selected elements.

the phase distribution imposed by the two-step MH synthesis. From the combined analysis of STEM-EDS, the average compositions were 75.7 % Ce / 24.3 % Zr and 72.1 % Ce / 27.9 % Zr for pZC and pCZ, respectively. The CZ sample showed a more homogeneous phase distribution without a clear distinction between ceria and zirconia in the analyzed regions. The CZ measured average composition is 78 % Ce / 22 % Zr. Chemical analysis of ceria-zirconia 2:1 samples by WDX revealed average compositions of 73.0 % Ce / 27.0 % Zr, 71.8 % Ce / 28.2 % Zr, and 75.3 % Ce / 24.7 % Zr for pZC, pCZ and CZ, respectively, in good agreement with STEM-EDS and Rietveld refinement data.

Both crystallographic and structural characterization provided valuable insights to identify the effect of the electrocatalyst assembly method. It is confirmed that by controlling the addition of the metal oxide precursors during the synthesis, it was possible to produce different configurations of ceria and zirconia phases in ceria-zirconia nanoparticles with comparable chemical composition, particle size, and morphology.

To further investigate the surface composition of the electrocatalysts, XPS spectra of the ceria-zirconia 2:1 samples were collected (Fig. 5). The Ce 3d high-resolution spectra in Fig. 5a show the two multiplets (v and u) corresponding to the spin–orbit split $3d_{5/2}$ and $3d_{3/2}$ core holes of CeO_2. Ten peaks corresponding to the pairs of spin–orbit doublets can be identified in the Ce $3d_{3/2,5/2}$ spectra of the studied samples, which agree with previously reported data [25]. Such peaks were fitted to the corresponding states $Ce^{3+}$and Ce^{4+}. All nanoparticles showed the typical Zr 3d spectra, as shown in Fig. 5b. For the Zr 3d analysis, well-resolved spin–orbit doublets ($d_{5/2}$ and $d_{3/2}$), separated by ~ 2.4 eV, indicate the formation of ZrO_x. The Zr 3d doublet peaks have 182.3 eV and 184.7 eV, corresponding to contributions from Zr $3d_{5/2}$ and Zr $3d_{3/2}$, respectively.

The surface elemental composition of the electrocatalysts was calculated according to the normalized peak areas of the Ce 3d and Zr 3d core level spectra, listed in Table 1. The results in Table 1 correspond to the average fitted values of at least three measured spectra collected in different samples of the same batch. It is interesting to note that XPS data clearly reflects the assembly of the nanoparticles. As the photoelectrons probe only a few layers of the samples, the fitted compositions indicate the most exposed species at the outer surface of the nanoparticles. Thus, sample pZC, in which initially formed Zr particles are then covered with ceria nanoparticles, exhibits the highest ceria fraction (Ce^{3+}+ Ce^{4+}), Ce:Zr = 2.2, as inferred by XPS data. The relative surface content of Ce^{3+} (4.6 atm%) for pZC indicates that this material has a large number of oxygen vacancies on its surface and a high oxygen mobility/storage because Ce^{3+} is associated with the formation of oxygen vacancies [26–30]. Conversely, the pCZ specimen shows the lowest value of the Ce:Zr = 0.67 ratio, with the lowest concentration of ceria (Ce^{3+} 2.8 atm % and Ce^{4+} 7.4 atm%). Interestingly, the solid solution sample CZ has a Ce:Zr = 2.1, which corresponds to the nominal stoichiometry with the highest amount of Ce^{3+}(4.8 atm%). Such a feature is related to the

Table 1
Surface elemental composition calculated according to normalized peak areas of the Ce 3d and Zr 3d XPS data.

Sample	Ce:Zr	Zr	Ce^{3+}	Ce^{4+}
pZC	2.2	8.4	4.6	13.8
pCZ	0.67	15.1	2.8	7.4
CZ	2.1	7.0	4.8	9.8

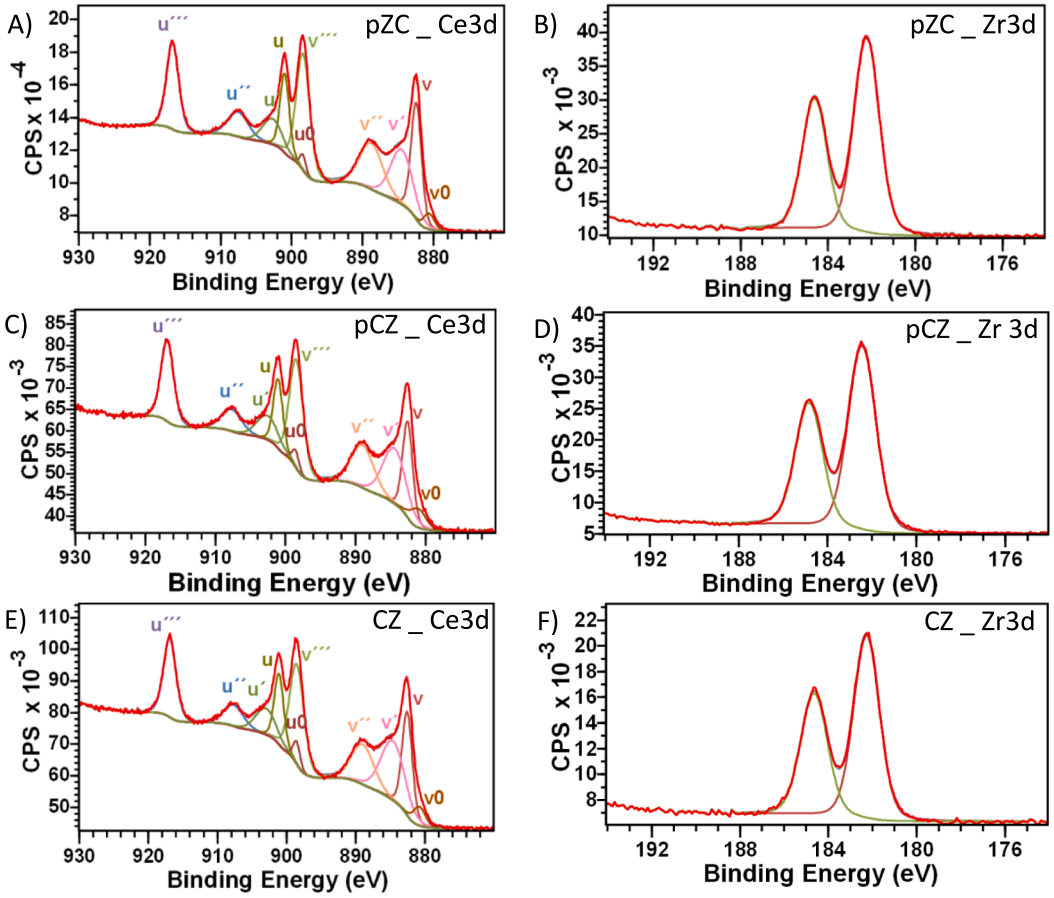

Fig. 5. XPS spectra of the ceria-zirconia samples (2:1): The left panel corresponds to Ce $3d_{3/2,\ 5/2}$ spectra, and the right panel to the Zr 3d spectra collected for the samples pZC (A, B), pCZ (C, D) and CZ (E, F).

formation of ceria-zirconia solid solutions, which were previously shown to exhibit an increased amount of Ce^{3+} as compared to pure ceria, as inferred by X-ray absorption synchrotron measurements [31].

The combined results of XRD, XPS, and TEM-EDS revealed that the assembling of ceria and zirconia nanoparticles resulted in electrocatalysts with distinct features, such as phase separation, surface composition, and active defects such as oxygen vacancy concentration that are crucial for tunning the methane conversion reactions.

3.2. Electrochemical conversion of methane

Considering that CeO_2 was previously shown as an active electrocatalyst for methane oxidation reaction, we have hypothesized that the ZrO_2 acts as a modifier to enhance selectivity to partially oxygenated compounds. Thus, we chose to perform the electrocatalytic characterization of samples pZC, pCZ, and CZ with Ce:Zr ratio of 2:1 and compare them with single-phase CeO_2 and ZrO_2 electrocatalysts. The reaction was initially assessed by determining the peak potentials toward methane oxidation obtained from cyclic voltammetry runs. The experiments were carried out in a methane-saturated medium (batch mode), using a previous run in a nitrogen-saturated medium (i.e., no methane) as a blank, which was subtracted from the methane run. Fig. 6 displays the voltammograms obtained for the ceria-zirconia samples with 2:1 ratio, along with the reference voltammograms of the individual oxides.

Different methane electrooxidation profiles were characterized by the presence of a process with onset potential (E_{onset}) at ~ 1.2 V followed by faradaic processes in the 1.4–1.6 V range and ~ 1.9 V vs. Ag/AgCl.

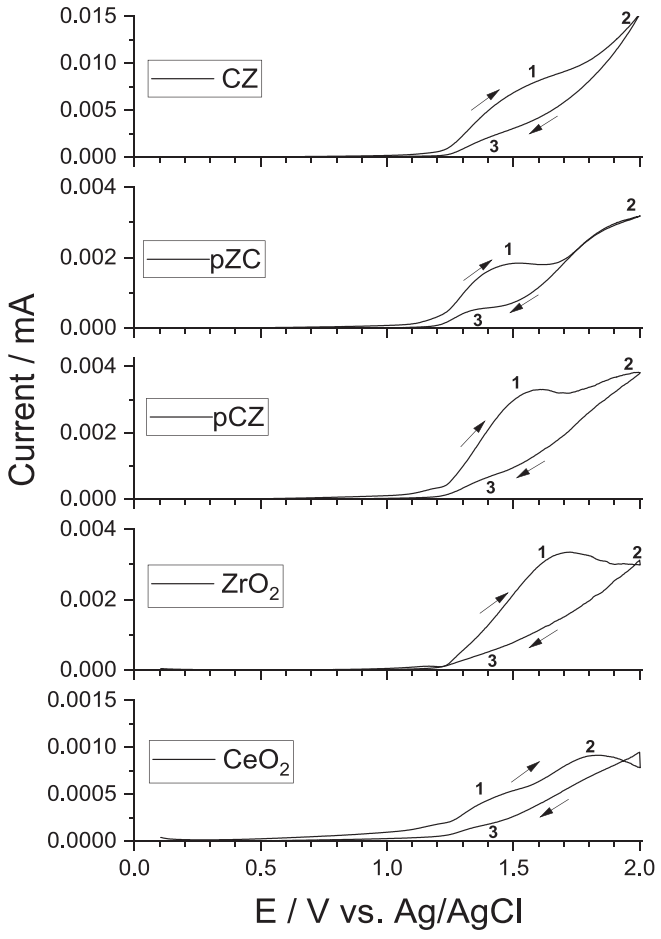

Fig. 6. Cyclic voltammograms of the methane oxidation on pZC, pCZ, and CZ electrocatalysts with Ce:Zr = 2:1 obtained in Na_2CO_3 0.1 mol/L and υ=50 mV s^{-1} versus Ag/AgCl. Data for CeO_2 and ZrO_2 are shown as a reference.

The E_{onset} process at 1.2 V can be attributed to the methane activation followed by partial oxidation, with the formation of methyl radicals (labeled as "1″ in Fig. 6). The methyl radicals are precursors for C1 and C2 compounds, such as methanol, ethanol, and acetaldehyde [20,32], which can further react with methane to form C3 compounds.

A continuous current increase with increasing potential characterizes the process starting from ~ 1.7 V (labeled as "2″ in Fig. 6). It can be the result of a continuous methane and/or intermediates oxidation with the oxygen evolution reaction (OER) taking place concomitantly [6]. The onset and peak potentials extracted from cyclic voltammograms for each catalyst are listed in Table S5.

Initially, individual CeO_2 and ZrO_2 were active electrocatalysts, and, surprisingly, ZrO_2 presented appreciable electrocatalytic activity, i.e., it exhibited a noticeable faradaic current. This finding is a strong indication that ZrO_2 facilitates CO_3^{2-} absorption [14] as the main responsible for the methane activation, and probably the carbonate adsorption is the rate-determining step for the formation of C1 and C2 compounds. A similar behavior is seen in all CeO_2:ZrO_2 samples, though more pronounced in the CZ electrocatalyst, which achieved relatively high current values comparable to that of CeO_2 and 4 to 10 times higher than those observed for the other samples.

The oxidation peak (labeled as "3″ in Fig. 6) in the cathodic scan at ~ 1.35 V is possibly associated with the oxidation of an intermediate (or a product) of the process related to peak 1. It suggests the re-oxidation of some intermediate or product of the first process (i.e., methane oxidation). It is consistent with the formation of intermediates resulting from partial oxidation of methane, which can lead to C2 + products. The intensity of the third process (peak 3) follows the sequence pZC > pCZ ~ CZ, indicating that more CeO_2 exposed at the surface (as in the pZC sample) favors partial methane oxidation.

Interestingly, such peak potentials reflect the values observed for the individual oxides. For ceria, peaks are observed at ~ 1.2 V and 1.5 V, while for zirconia, peaks are observed at 1.2 V and 1.7 V. These values are consistent with those obtained for the mixed oxides (pCZ and pZC) and the solid solution (CZ) electrocatalysts. The pZC 2:1 sample, characterized by a high amount of ceria grown on zirconia, exhibited the same potential as pure ceria for the second peak. In contrast, the pCZ 2:1 sample, which is zirconia grew over ceria support, displayed an intermediate second peak at 1.6 V, similar to the CZ solid solution. This behavior suggests that the catalysts are indeed bifunctional catalysis since both CeO_2 and ZrO_2 are playing a role in the oxidation path.

Considering the electric potential, a shift to more negative potentials is observed for bifunctional electrocatalysts, i.e., containing ceria in the composition. Such shift is not observed for ZrO_2, revealing that CeO_2 has a significant catalytic effect in methane oxidation. Such a feature suggests that ZrO_2 acts in the methane activation, while CeO_2 favors the methane electrooxidation at lower potentials.

Chronoamperometric curves are depicted in Fig. S2. The time dependence of the current at fixed potential showed a slight increase in all experiments, suggesting an activation process (Fig. S2). More importantly, all catalysts showed negligible changes during the experiments, indicating that the stability of the catalyst was maintained for 4 h.

The electrochemical processes involved in methane oxidation were identified through product analysis using the GC–MS technique at1.2 V and 1.6 V fixed potential, selected based on the onset and peak potentials shown in Fig. 6. Fig. S3 and Table S6 present the screening results obtained for each studied electrocatalyst, displaying the formed products and their respective quantification limits. The GC–MS measurements were conducted after 60 min of reaction with applied potential associated with the onset of anodic current (~1.2 V). Methanol, ethanol, and acetone were the main detected products. Quantified concentrations of methanol ranged from 129.7 to 758.8 μmol $g^{-1}h^{-1}$, ethanol from 97.4 to 459.8 μmol $g^{-1}h^{-1}$, and acetone was formed in smaller amounts, ranging from 77.7 to 134.0 μmol $g^{-1}h^{-1}$, depending on both the microstructure and relative composition.

Calculated Faradaic efficiencies (η) varied from 0.1 to 17.4 % and showed a clear maximum for the CeO_2:ZrO_2 2:1 composition, regardless of the microstructural configuration of the electrocatalyst. Samples with CeO_2:ZrO_2 ratios of 1:1 and 1:2 exhibited maximum η = 4 %, while samples with a 2:1 ratio demonstrated higher product formation efficiencies (η up to 18 %). Nonetheless, high amounts of methanol were converted by the pCZ (758.8 mmol $g^{-1}h^{-1}$) and pZC (403.8 mmol $g^{-1}h^{-1}$) electrocatalysts with 1:1 CeO_2:ZrO_2 ratio with considerable low η ~ 0.5 %. However, the striking result is the total η ~ 48 % for methane conversion to methanol, ethanol, and acetone measured for the pZC with 2:1 CeO_2:ZrO_2 ratio, which indicates a high selectivity.

The microstructural analyses showed that the pZC sample has a significant CeO_2 amount on the surface, confirming the critical role of the ceria in the methane electrooxidation activity. In addition, XPS data (Fig. 5) have shown that the main difference between pCZ and pZC is related to the amount of Ce^{3+} species on the surface. The presence of Ce^{3+} species is related to the oxygen vacancies ($V_{\dot{O}}$) concentration, which has a strong redox catalytic effect. This finding can be evidenced by the shift towards more negative potentials (Fig. 6) for bifunctional catalysts in comparison to ZrO_2, demonstrating that the methane conversion is thermodynamically facilitated in the presence of CeO_2.

Since the catalysts with ceria: zirconia ratio of 2:1 have demonstrated the highest Faradaic efficiencies, they were selected to evaluate the electrooxidation of methane under different applied potentials, with the results detailed in Fig. 7 and Table S7.

Fig. 7 shows that a large amount of Ce^{3+} at the surface in sample pZC contributes to a high Faradaic efficiency. In contrast, the high selectivity to methanol of sample pCZ indicates that selectivity requires a more subtle balance between zirconia and ceria. A clear correlation is observed between the magnitude of the electrical current and the shift towards more negative potentials with increasing Ce^{3+} ion contents. This increase is indicative of more oxygen vacancies, which facilitate methane electrooxidation at ambient temperature. Interestingly, the ceria-zirconia solid solution (CZ) sample exhibited lower electrochemical activity, which underscores the beneficial effects of having ceria and zirconia in a phase-separated configuration for this reaction. The phase arrangement appears to be critical for optimizing the electrooxidation of methane, even in the face of a substantial concentration of oxygen vacancies within the solid solution. Thus, the experimental results indicate that carbonate ions on ZrO_2 surface act primarily in the activation and as an oxygen donor for the oxygenation of the intermediate species resulting from activation and partial oxidation processes [33], contributing effectively to selectivity. CeO_2, in contrast, seems to offer an electrocatalytic effect, enhancing Faradaic efficiency. The coexistence of Ce^{3+} in segregated phase catalysts like pZC and pCZ may lead to improved performance due to kinetic modifications in redox reactions. Since both oxygen vacancy formation and methane adsorption on ceria are surface reduction processes, the activation energy required for methane oxidation is directly associated with the reducibility of ceria [34–36].

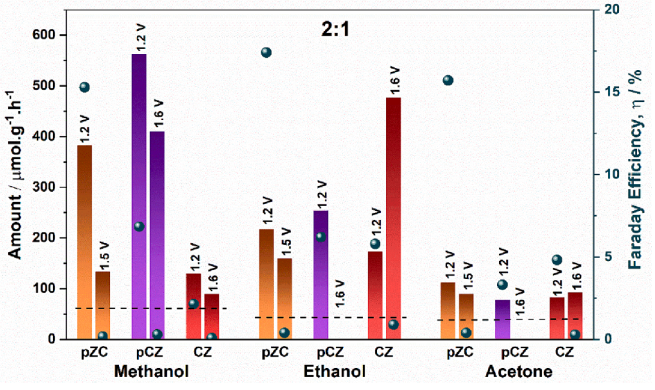

Fig. 7. Quantification of the products generated by the electrooxidation of methane using the catalysts pZC, pCZ, and CZ in the 2:1 ratio varying the applied potential (see Tables SI-5 and SI-6) in Na_2CO_3 0.1 mol/L versus Ag/AgCl.

Summarily, it was observed that catalysts with a mix of both cerium and zirconium oxides favored the initial methane conversion reactions more than the solid solution catalysts (CZ sample). Zirconium dioxide was particularly critical in the early reaction stages, offering active sites for both carbonate ion formation and methane activation. As the reaction progressed, the formation of methyl radicals was a precursor to creating longer-chain alcohols (C2 + alcohols). The catalyst pZC, which had a higher surface concentration of cerium, showed optimal selectivity and Faradaic efficiency. It is attributed to the surface's oxygen-active species, which are linked to the mobility of lattice oxygen and the presence of Ce^{3+} ions, creating necessary oxygen vacancies. The synergy between zirconium and cerium oxides on the catalyst surface is crucial, as it facilitates both the adsorption and activation stages of the reaction. However, a balance is necessary to prevent over-oxidation; a controlled presence of active oxygen species is essential to promote mild oxidation rather than complete oxidation to CO_2.

For pZC and pCZ materials, the onset potential 1.2 V provided the highest conversions and Faradaic efficiencies. Increasing the applied potential to the peak at 1.6 V decreased conversion rates, and Faradaic efficiency dropped to η < 2 %, possibly indicating a predominance of the oxygen evolution reaction (Eq. 2) over the methane oxidation. Nevertheless, it's worth noting that at 1.6 V, a high selectivity was achieved for methanol formation in the pCZ electrocatalyst, while the CZ sample displayed the highest selectivity for ethanol.

Methanol is the main product of methane conversion (Fig. 7); however, both ethanol and acetone are also detected in appreciable concentrations. Table 2 presents the possible reactions involved in the methane conversion by using CeO_2-ZrO_2 bifunctional electrocatalysts. Equation 2 is associated with OER, and Equations 3–8 detail the reactions involved for all possible products found in the electrooxidation of methane using the synthesized materials. Equation 3 refers to complete methane oxidation, while Equations 4–8 are related to the partial methane oxidation processes, which are reactions of interest from methane to value-added products, forming methanol, ethanol, acetaldehyde, isopropanol, and acetone. The dissociative adsorption of methane occurs through the abstraction of an H atom, forming a methyl radical ($CH_4 \rightarrow CH_3\bullet + H^+ + 1e^-$), while a surface metal atom is reduced by a single electron ($Ce^{4+} + 1e^- \rightarrow Ce^{3+}$) [34]. Incorporating metal atoms such as Zr on the surface reduces the oxygen vacancy formation energy and the activation energy barrier for methane adsorption [37].

The methane conversion is assumed to start with the methane activation to CH_3*, following conversion to C2 + products. The product selectivity is based on the phase composition and surface properties of the ceria-zirconia (CeO_2-ZrO_2) electrocatalysts. The presence of Ce^{3+} and the associated oxygen vacancies, particularly enhanced in the pZC (preformed ZrO_2 with CeO_2 addition) samples, play a crucial role in

Table 2
Possible products found in electrooxidation of methane using CeO_2/ZrO_2 bifunctional electrocatalysts.

Possible occurring reactions		
Oxygen evolution reaction	$2H_2O \rightarrow O_2 + 4H^+ + 4e^-$	Eq. 2
Complete Methane oxidation	$CH_4 + CO_3^{2-} \rightarrow CO_2 + CO + 2H_2 + 2e^-$	Eq. 3
Possible reactions for C2 + products' formation		
Methanol	$CH_4 + CO_3^{2-} \rightarrow CH_3OH + CO_2 + 2e^-$	Eq. 4
Ethanol	$CH_4 + CH_3OH + CO_3^{2-} \rightarrow CH_3CH_2OH + H_2O + CO_2 + 2e^-$	Eq. 5
Acetaldehyde	$CH_3CH_2OH + CO_3^{2-} \rightarrow CH_3CHO + CO_2 + H_2O + 2e^-$	Eq. 6
Isopropanol	$CH_4 + CH_3CHO \rightarrow CH_3CHCH_3OH$	Eq. 7
Acetone	$CH_3CHCH_3OH + CO_3^{2-} \rightarrow CH_3COCH_3 + CO_2 + H_2O + 2e^-$	Eq. 8

facilitating methane activation at lower potentials, leading to increased Faradaic efficiency. Thus, the formation of the different products is kinetically controlled by the diffusion of the species and by their different affinities with the catalyst surfaces. It was observed that carbonate ions on ZrO_2 surface act primarily in the activation and as an oxygen donor for the oxygenation of the intermediate species resulting from activation and partial oxidation processes. The pCZ system (preformed ceria nanoparticles with zirconia addition at the surface), since we expect a higher exposition of ZrO_2, leads to higher methanol production that confirms the methane activation, but possibly a low adsorption at the surface. The best activity of the pZC catalyst (in terms of faradaic efficiency and of C2 + production) is thus explained by the effective synergy between the activation roles of carbonate ions on ZrO_2, enhancing methane activation and oxygen donation, and the electrocatalytic effects of CeO_2, which boost Faradaic efficiency through the formation and mobility of oxygen vacancies and active oxygen species. It is noteworthy that the product selectivity for pZC follows the sequence methanol > ethanol > acetone, i.e., C1 > C2 > C3, supporting that C2 + products are generated by reactions of CH_3* with as-formed methanol.

Monitoring the production of CO_2 is essential to understand the conversion performance. Partial electrooxidation to methanol or other products of interest remains a critical issue, mainly because methane can be fully oxidized to CO_2 even under mild oxidizing conditions. Usually, conversion products are far more reactive than methane and end up overoxidized. Consequently, few catalysts can prevent excessive oxidation to carbon dioxide (CO_2) or other CO_x compounds. The intermediate products are easily activated once the high activation energy is provided for dissociating the methane's C-H bond. [8–12]. As highlighted by Equation 3, the direct conversion of methane to CO_2 is energetically favored since a $E^\circ = 0.17$ V is required.

Therefore, the evaluation of the two applied potentials on the performance of methane oxidation shows that the reactions of total conversion to CO_2, the re-oxidation of products, and oxygen evolution reactions become predominant when higher potentials are applied, reducing both product formation and the Faradaic efficiency of the process.

Fig. S4 shows the selectivity determined from the quantities of products obtained for each electrocatalyst, using a loading of 1 mg.cm^{-2}. In Table 3, selectivity is compared to Faradaic efficiency.

Upon examining the interplay between selectivity and Faradaic efficiency in the studied electrocatalysts, it is found that high selectivity is achievable, though it tends to coincide with reduced methane conversion rates. The high selectivity is reflected in the estimated CH_4 conversion, detailed in Table S6, which shows that the highest conversions do not correspond to the best Faradaic efficiencies. The electrocatalyst pCZ with a 2:1 ratio stands out, achieving a methanol formation efficiency of 6.9 % at a selectivity of 63 %, while the CZ with a similar ratio yields ethanol with a 5.8 % efficiency and 45 % selectivity. Not far behind in performance is the 2:1 pZC configuration, which achieves a methanol selectivity of 54 % and an impressive efficiency of 15.3 %. Additionally, this material also shows promising results for ethanol, with a selectivity of 31 % and an efficiency of 17.4 %.

Table 3
Selectivity and Faradaic efficiency of pZC, pCZ, and CZ 2:1 electrocatalysts for methanol, ethanol, and acetone using a 1 mg.cm^{-2} catalyst loading and onset potential of 1.2 V.

Sample	Methanol		Ethanol		Acetone	
Ce:Zr 2:1	Selectivity (%)	η (%)	Selectivity (%)	η (%)	Selectivity (%)	η (%)
pZC	54	15.3	31	17.4	16	15.7
pCZ	63	6.9	28	6.3	9	3.3
CZ	34	2.2	45	5.8	21	4.8

4. Conclusion

The comprehensive analysis of ceria-zirconia electrocatalysts by advanced characterization techniques such as X-ray diffraction (XRD), electron microscopy, and X-ray photoelectron spectroscopy (XPS) has elucidated the crucial role of phase composition and surface properties in methane electrooxidation. The experimental findings underscore the importance of phase separation of ceria and zirconia for optimizing catalytic performance. Notably, the presence of Ce^{3+} and the associated oxygen vacancies, which are enhanced in the pZC samples, are instrumental in facilitating methane conversion at lower potentials, leading to increased faradaic efficiency. The optimal balance between ceria and zirconia phases, particularly in a 2:1 ratio, is determinant in achieving high selectivity and efficiency in electrocatalytic applications, as evidenced by the superior performance of pZC and pCZ electrocatalysts in the selective formation of methanol and ethanol. In conclusion, the strategic assembly of ceria-zirconia nanoparticles significantly influences the electrocatalytic activity, with the electrochemical behavior being closely linked to the surface composition and the presence of active defects, such as oxygen vacancies and active adsorption sites. The findings of this study provide a pathway for the design of highly efficient and selective electrocatalysts for methane oxidation. Moreover, it contributes to the broader understanding of the interplay between material synthesis, microstructure, and electrocatalytic performance. Future work should aim to refine the synthesis process further to control the surface characteristics and phase distribution, which are pivotal in tailoring the catalytic properties for desired electrochemical reactions.

CRediT authorship contribution statement

Nicole Boghosian Patricio: Writing – original draft, Investigation, Formal analysis. **Juliano Carvalho Cardoso:** Writing – original draft, Methodology, Investigation, Formal analysis, Data curation. **Márcia Tsuyama Escote:** Formal analysis. **Alexandre José de Castro Lanfredi:** Writing – review & editing, Investigation, Formal analysis. **Abhaya Datye:** Formal analysis. **Hien Pham:** Formal analysis. **Caue Ribeiro:** Writing – review & editing, Formal analysis. **Fabio Coral Fonseca:** Writing – review & editing, Project administration, Investigation, Funding acquisition. **Elisabete Inacio Santiago:** Writing – review & editing, Project administration, Methodology, Investigation, Formal analysis, Conceptualization.

Declaration of competing interest

The authors declare the following financial interests/personal relationships which may be considered as potential competing interests: Fabio Coral Fonseca reports financial support was provided by State of Sao Paulo Research Foundation. Fabio Coral Fonseca reports financial support was provided by National Council for Scientific and Technological Development. If there are other authors, they declare that they have no known competing financial interests or personal relationships that could have appeared to influence the work reported in this paper.

Data availability

Data will be made available on request.

Acknowledgments

The authors are grateful for the support of the Center for Innovation on New Energies (CINE) - SHELL (ANP) / FAPESP grant No. 2017/11937- 4, Conselho Nacional de Desenvolvimento Científico e Tecnológico (CNPq) SiS-H2 407967/2022-2 and scholarship 409792/2018-7. NSF DMR-1828731 supported the acquisition of the AC-STEM at UNM. The authors also acknowledge the Laboratory of Advanced Materials (UFABC) for the use of their Microwave Reaction System and all facilities, the Multi-User Center (UFABC) for the use of XRD and FEG-

SEM equipment, and Functional Materials Development Center CDMF/UFSCar for the TEM facilities, FAPESP grant No. 2013/07296-2. CR also acknowledges FAPESP grant 18/01258-5 and CNPq grants 442575/2019-0 and 406925/2022-4. CR, FCF and EIS are fellows of the Brazilian CNPq.

Appendix A. Supplementary data

Supplementary data to this article can be found online at https://doi.org/10.1016/j.cej.2024.150951.

References

[1] M. Ravi, M. Ranocchiari, J.A. van Bokhoven, Die direkte katalytische Oxidation von Methan zu Methanol - eine kritische Beurteilung, Angew. Chem. 129 (2017) 16684–16704, https://doi.org/10.1002/ange.201702550.
[2] Z. Zakaria, S.K. Kamarudin, Direct conversion technologies of methane to methanol: An overview, Renew. Sustain. Energy Rev. 65 (2016) 250–261, https://doi.org/10.1016/j.rser.2016.05.082.
[3] P.V.L. Reddy, K.H. Kim, H. Song, Emerging green chemical technologies for the conversion of CH4 to value added products, Renew. Sustain. Energy Rev. 24 (2013) 578–585, https://doi.org/10.1016/j.rser.2013.03.035.
[4] U., Energy Information Administration, International Energy, Outlook (2019, 2019.) www.eia.gov/ieo.
[5] T.J. Omasta, W.A. Rigdon, C.A. Lewis, R.J. Stanis, R. Liu, C.Q. Fan, W.E. Mustain, Two Pathways for Near Room Temperature Electrochemical Conversion of Methane to Methanol, ECS Trans. 66 (2015) 129–136, https://doi.org/10.1149/06608.0129ecst.
[6] L. Arnarson, P.S. Schmidt, M. Pandey, A. Bagger, K.S. Thygesen, I.E.L. Stephens, J. Rossmeisl, Fundamental limitation of electrocatalytic methane conversion to methanol, PCCP 20 (2018) 11152–11159, https://doi.org/10.1039/c8cp01476k.
[7] P.G. Lustemberg, R.M. Palomino, R.A. Gutiérrez, D.C. Grinter, M. Vorokhta, Z. Liu, P.J. Ramírez, V. Matolín, M.V. Ganduglia-Pirovano, S.D. Senanayake, J. A. Rodriguez, Direct Conversion of Methane to Methanol on Ni-Ceria Surfaces: Metal-Support Interactions and Water-Enabled Catalytic Conversion by Site Blocking, J. Am. Chem. Soc. 140 (2018) 7681–7687, https://doi.org/10.1021/jacs.8b03809.
[8] B. Wang, S. Albarracín-Suazo, Y. Pagán-Torres, E. Nikolla, Advances in methane conversion processes, Catal. Today 285 (2017) 147–158, https://doi.org/10.1016/j.cattod.2017.01.023.
[9] V. V. Thyssen, V. B. Vilela, D.Z. de Florio, A.S. Ferlauto, F.C. Fonseca, Direct Conversion of Methane to C2 Hydrocarbons in Solid-State Membrane Reactors at High Temperatures, Chemical Reviews 122 (3), 3966-3995. https://doi.org/10.1021/acs.chemrev.1c00447.
[10] C. Mesters, A Selection of Recent Advances in C1 Chemistry, Annu Rev Chem Biomol Eng 7 (2016) 223–238, https://doi.org/10.1146/annurev-chembioeng-080615-034616.
[11] K.J. Lee, J.L. Dempsey, When Electrochemistry Met Methane: Rapid Catalyst Oxidation Fuels Hydrocarbon Functionalization, ACS Cent. Sci. 3 (2017) 1137–1139, https://doi.org/10.1021/acscentsci.7b00469.
[12] A.H. Bagherzadeh Mostaghimi, T.A. Al-Attas, M.G. Kibria, S. Siahrostami, A review on electrocatalytic oxidation of methane to oxygenates, J Mater Chem A Mater 8 (2020) 15575–15590, https://doi.org/10.1039/d0ta03758c.
[13] J.A. Arminio-Ravelo, M. Escudero-Escribano, Strategies toward the sustainable electrochemical oxidation of methane to methanol, Curr Opin Green Sustain Chem 30 (2021), https://doi.org/10.1016/j.cogsc.2021.100489.
[14] N. Spinner, W.E. Mustain, Electrochemical Methane Activation and Conversion to Oxygenates at Room Temperature, J. Electrochem. Soc. 160 (2013) F1275–F1281, https://doi.org/10.1149/2.071311jes.
[15] M.S.A. Sher Shah, C. Oh, H. Park, Y.J. Hwang, M. Ma, J.H. Park, Catalytic Oxidation of Methane to Oxygenated Products, in: Recent Advancements and Prospects for Electrocatalytic and Photocatalytic Conversion at Low Temperatures, Advanced Science 7, 2020, https://doi.org/10.1002/advs.202001946.
[16] B. Christian Enger, R. Lødeng, A. Holmen, A review of catalytic partial oxidation of methane to synthesis gas with emphasis on reaction mechanisms over transition metal catalysts, Appl Catal A Gen 346 (2008) 1–27, https://doi.org/10.1016/j.apcata.2008.05.018.
[17] N. Xu, C.A. Coco, Y. Wang, T. Su, Y. Wang, L. Peng, Y. Zhang, Y. Liu, J. Qiao, X. D. Zhou, Electro-conversion of methane to alcohols on “capsule-like” binary metal oxide catalysts, Appl Catal B 282 (2021), https://doi.org/10.1016/j.apcatb.2020.119572.
[18] M. Ma, C. Oh, J. Kim, J.H. Moon, J.H. Park, Electrochemical CH4 oxidation into acids and ketones on ZrO2:NiCo2O4 quasi-solid solution nanowire catalyst, Appl Catal B 259 (2019), https://doi.org/10.1016/j.apcatb.2019.118095.
[19] P. Burroughs, A. Hamnett, A.F. Orchard, G. Thornton, Satellite structure in the X-ray photoelectron spectra of some binary and mixed oxides of lanthanum and cerium, Journal of the Chemical Society, Dalton Trans. (1976) 1686–1698, https://doi.org/10.1039/DT9760001686.
[20] M. Ma, B.J. Jin, P. Li, M.S. Jung, J. Il Kim, Y. Cho, S. Kim, J.H. Moon, J.H. Park, Ultrahigh Electrocatalytic Conversion of Methane at Room Temperature, Advanced Science 4 (2017), https://doi.org/10.1002/advs.201700379.
[21] W.Z. Zhu, S.C. Deevi, A review on the status of anode materials for solid oxide fuel cells, Mater. Sci. Eng. A 362 (2003) 228–239, https://doi.org/10.1016/S0921-5093(03)00620-8.
[22] T. Guo, J. Du, J. Li, The effects of ceria morphology on the properties of Pd/ceria catalyst for catalytic oxidation of low-concentration methane, J. Mater. Sci. 51 (2016) 10917–10925, https://doi.org/10.1007/s10853-016-0303-z.
[23] M. Chrzan, D. Chlebda, P. Jodłowski, E. Salomon, A. Kołodziej, A. Gancarczyk, M. Sitarz, J. Łojewska, Towards Methane Combustion Mechanism on Metal Oxides Supported Catalysts: Ceria Supported Palladium Catalysts, Top. Catal. 62 (2019) 403–412, https://doi.org/10.1007/s11244-019-01143-8.
[24] S.H. Kye, H.S. Park, R. Zhang, H.J. Yang, K.H. Lee, H. Suh, J.G. Kim, M.G. Kim, G. S. Hwang, N.H. Hur, Partial oxidation of methane to methanol by isolated Pt catalyst supported on a CeO2 nanoparticle, J. Chem. Phys. 152 (2020), https://doi.org/10.1063/1.5135741.
[25] E. Bèche, P. Charvin, D. Perarnau, S. Abanades, G. Flamant, Ce 3d XPS investigation of cerium oxides and mixed cerium oxide (Ce xTiyOz), in: In: Surface and Interface Analysis, 2008, pp. 264–267, https://doi.org/10.1002/sia.2686.
[26] C.M. Sims, R.A. Maier, A.C. Johnston-peck, J.M. Gorham, V.A. Hackley, B.C. Nelson, Quantitative Analysis of Oxidation State in Cerium Oxide Nanomaterials Material Measurement Laboratory , National Institute of Standards and Technology , 100 Bureau Drive , Gaithersburg , MD 20899 , USA Scanning Transmission Electron Microscopy (STEM) I, (n.d.) 1–4.
[27] V. Cortés Corberán, V. Rives, V. Stathopoulos, Recent Applications of Nanometal Oxide Catalysts in Oxidation Reactions, 2018. https://doi.org/10.1016/B978-0-12-814807-5.00007-3.
[28] A.D. Mayernick, M.J. Janik, Methane activation and oxygen vacancy formation over CeO2 and Zr, Pd substituted CeO2 surfaces, J. Phys. Chem. C 112 (2008) 14955–14964, https://doi.org/10.1021/jp805134s.
[29] J. Li, X. Liu, W. Zhan, Y. Guo, Y. Guo, G. Lu, Preparation of high oxygen storage capacity and thermally stable ceria-zirconia solid solution, Catal, Sci. Technol. 6 (2016) 897–907, https://doi.org/10.1039/c5cy01571e.
[30] L.P. Teh, H.D. Setiabudi, S.N. Timmiati, M.A.A. Aziz, N.H.R. Annuar, N.N. Ruslan, Recent progress in ceria-based catalysts for the dry reforming of methane: A review, Chem. Eng. Sci. 242 (2021) 116606, https://doi.org/10.1016/j.ces.2021.116606.
[31] F. Zhang, C.H. Chen, J.M. Raitano, J.C. Hanson, W.A. Caliebe, S. Khalid, S. W. Chan, Phase stability in ceria-zirconia binary oxide nanoparticles: The effect of the Ce3+ concentration and the redox environment, J. Appl. Phys. 99 (2006), https://doi.org/10.1063/1.2190712.
[32] I. Bar-Nahum, A.M. Khenkin, R. Neumann, Mild, aqueous, aerobic, catalytic oxidation of methane to methanol and acetaldehyde catalyzed by a supported bipyrimidinylplatinum-polyoxometalate hybrid compound, J. Am. Chem. Soc. 126 (2004) 10236–10237, https://doi.org/10.1021/ja0493547.
[33] N. Spinner, W.E. Mustain, Influence of Non-Conducting Zirconia on the Electrochemical Performance of Nickel Oxide in Alkaline Media at Room Temperature, J. Electrochem. Soc. 159 (2012) E187–E192, https://doi.org/10.1149/2.051212jes.
[34] K. Reed, A. Cormack, A. Kulkarni, M. Mayton, D. Sayle, F. Klaessig, B. Stadler, Exploring the properties and applications of nanoceria: Is there still plenty of room at the bottom?, Environ Sci, Nano 1 (2014) 390–405, https://doi.org/10.1039/c4en00079j.
[35] J. Xu, X. Xiao, J. Zhang, J. Liu, J. Ni, H. Xue, H. Pang, Oxygen Vacancies Enhancing Electrocatalysis Performance of Porous Copper Oxide, Part. Part. Syst. Char. 34 (2017), https://doi.org/10.1002/ppsc.201600420.
[36] A. Badreldin, A.E. Abusrafa, A. Abdel-Wahab, Oxygen-Deficient Cobalt-Based Oxides for Electrocatalytic Water Splitting, ChemSusChem 14 (2021) 10–32, https://doi.org/10.1002/cssc.202002002.
[37] A. Barroso-Bogeat, B. Núñez-Pérez, G. Blanco, J.M. Pintado, J.C. Hernández-Garrido, J.J. Calvino, Surface and redox characterization of new nanostructured ZrO2@CeO2 systems with potential catalytic applications, Surf. Interface Anal. 50 (2018) 1025–1029, https://doi.org/10.1002/sia.6444.